MDPI

Article

The Effect of Macroscopic Particle Features on Mineral Dissolution

Chandra Widyananda Winardhi *, Jose Ricardo da Assuncao Godinho and Jens Gutzmer [ID]

Helmholtz Zentrum Dresden-Rossendorf, Helmholtz Institut Freiberg for Resource Technology, Chemnitzer Str. 40, 09599 Freiberg, Germany
* Correspondence: c.winardhi@hzdr.de

Abstract: Mineral dissolution is a dynamic process in which kinetics depend on the reactive surface area, orientation, and geometry of the dissolving mineral grain. Dissolution rate is, thus, not represented by a single value, but rather, by a spectrum that is affected by the reactivity of different types of surface features. Such dissolution rate spectra are usually obtained by very detailed studies of perfectly cleaved surfaces by atomic force microscopy or in situ studies, such as flow-through experiments. This study visualizes dissolution progress by repeated X-ray computed tomography scans of a single particle. This allows studying the influence of larger particle features, such as corners and edges, at the interception of macroscopic faces of particles, as well as the influence of those macroscopic features on the dissolution rate spectra. As a suitable case study, the dissolution of a monomineralic galena (PbS) particle in ethaline is studied. The observed changes in particle geometry are evaluated using a newly developed empirical model in order to break down the rate spectra as a function of the particle geometry. Results illustrate that dissolution rates are exponentially correlated with the distance to crystal corners and edges. The reactivity map generated from these exponential relations shows a linear trendline with the dissolution rates over the entire surface of the studied galena particle. The empirical reactivity map developed here opens the possibility of predicting the dissolution rate of particulate materials based on computed tomography and the optimal geometrical properties of the particles that maximize the dissolution, e.g., size and shape.

Keywords: computed tomography (CT); corners and edges; dissolution; dissolution rate spectra; reactivity map

1. Introduction

Mineral dissolution is involved in many natural geochemical processes (e.g., weathering or hydrothermal alteration) [1,2] and industrial processes (e.g., carbon capture sequestration or hydrometallurgical leaching) [3,4]. Dissolution rates are often estimated from element concentrations in resulting leachates [5,6]. However, dissolution is a dynamic process that depends not only on the solution (e.g., solvent concentration, temperature and fluid velocity) [7–9], but also on the solid properties, such as reactive surface area, surface orientation, and geometry [10]. Previous work has shown that dissolution rates are not constant across minerals [11–13], but they are better represented by a distribution of values that has been termed a dissolution rate spectrum [14].

Dissolution rate spectra were mostly studied by three-dimensional surface imaging methods, e.g., optical profiler [4,10,15] and atomic force microscopy [14,16]. It was shown that the surface orientation affects its reactivity, i.e., dissolution rate, due to differences in the number of reactive surface sites, such as atomic scale steps and kinks [10,17,18]. This experimental evidence was used to develop dissolution models based on the reactivity of surface sites [9,18,19]. Despite providing high spatial resolution, three-dimensional surface imaging methods usually require flat surfaces, e.g., polished or cleaved, and the observations are usually limited to very small regions on single planes. From such studies,

it is well known that the intersection of two or more crystal planes exceeds an important control on the crystal total dissolution [20]. At the same time, simultaneous investigation of macroscopic particle features remained an experimental challenge [21], as conventional three-dimensional surface imaging methods only allow observation of a single intersection at any given time.

In contrast to that, X-ray computed tomography (CT) can provide direct measurements of three-dimensional volumetric changes of minerals during dissolution [8,21–25]. Noiriel et al. recently documented that a millimeter-sized calcite crystal has higher dissolution rates along its particle corners and edges as compared to dissolution rates on crystal faces [22,23]. On both an atomic scale [11] and a macroscopic scale [23], these corners and edges are well known to increase the population of steps and kinks over time, as they will propagate. However, often the experiment used a flow-through column or a mixed-flow reactor, and hydrodynamic properties of the flow could affect the dissolution progress [9].

In order to address this shortage, the dissolution of millimeter-sized mineral grains/fragments, especially around particle corners and edges, is observed in this study, with the aim to determine realistic dissolution rate spectra. This knowledge can then be used to extend mineral dissolution models that are mostly derived from single surface experiments or from powder experiments (bulk dissolution) [26]. Models that account for particle geometry can constrain the variability of bulk mineral dissolution rates measured from thousands of particles stirred in a reactor that may be inconsistent in relation to those measured in the field [27]. Additionally, the results can be used to simulate the dissolution of multi-mineral particles during batch leaching experiments [26]. As a case study, the present investigation investigates the interaction between different macroscopic features of a mm-sized monomineralic galena grain during dissolution in ethaline. The influence of macroscopic features, such as particle corners and edges towards adjacent cleavage surfaces, are observed using CT. Furthermore, an empirical model is proposed to generate reactivity maps based on the distance to the macroscopic features in order to investigate the effects of particle geometry on dissolution rate spectra.

2. Materials and Methods

The four hypotheses tested in this study are: (a) dissolution observed on macroscopic features (particle corners and edges) formed at the interception of on the main planes of a particle, act as permanent sources of instability; (b) the additional instability ultimately translating into an increased local dissolution rate [28,29]; (c) empirical observations that can be used to calculate this local dissolution rate; (d) dissolution rate spectra can be used to calibrate a reactivity map solely from a particle's three-dimensional geometry, i.e., the distance from macroscopic features.

Figure 1 illustrates the motivation for this study. Bulk dissolution experiments performed in a laboratory use a large number of individual particles, each with a unique geometry (Figure 1a). Consequently, each particle has a specific dissolution rate, which has a unique evolution through time, following the changes of geometry of that specific particle (Figure 1b). The hypotheses formulated above are tested by dissolving one particle and using the measured dissolution rates to generate a surface reactivity map that is based on the particle geometry (Figure 1b). Such models can be used in the future to simulate dissolution in a multi-particle bulk dissolution experiment, where each particle has its own unique geometry. Our particle-level empirical model is compatible and complementary to existing mechanistic models [11]. For instance, macroscopic features affect the surface reactivity similarly to crystal spiral defects in the sense that they act as a permanent source of instability from where atomic scale step waves are emanated, as illustrated in Figure 1c. Here, one cube illustrates one unit cell in the crystal lattice and the red cubes highlight sites of high reactivity. However, an important difference is that macroscopic features affect different crystal planes in different directions. Consequently, a point on a surface may be affected by different macroscale features depending on its distance.
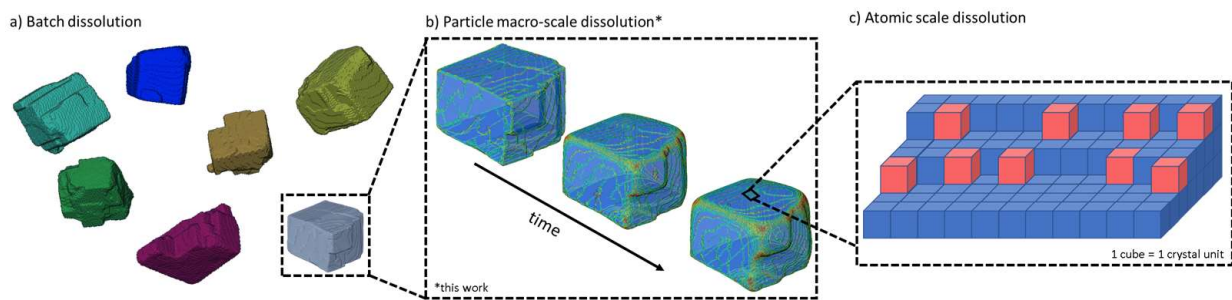
Figure 1. Illustration of the proposed concept, (**a**) bulk dissolution, i.e., batch leaching of multiple particles, each with unique geometry. (**b**) Each particle has a specific reactivity and dissolution rate map depending on its geometry (particle corners and edges). Warm color highlighting high reactivity on the corners and cold colors depicting low reactivity on the surface. (**c**) Our models are compatible with atomic scale mechanistic dissolution models, e.g., macroscopic edges have a similar effect as crystal spiral defects as sources of atomic step wave dissolution.

2.1. Materials and Sample Preparation

A monomineralic and nearly cube-shaped particle of galena (PbS) of ca. 2 mm size from Freiberg, Germany was studied. The sample was sourced from the Geoscientific Collections of the TU Bergakademie Freiberg (μXRF spectra of this sample are provided in the Supplementary Files, Figure S1, relating to this contribution). Galena is a sulfide mineral of typically very simple chemical composition, cubic symmetry, and perfect cleavage along the {100} crystal planes (Figure 1). One cleavage surface of the particle was coated with epoxy resin prior to the dissolution experiment (orange in Figure 2) to prevent dissolution along this surface, allowing its use as a reference for registration of CT images. The other five {100} cleavage planes were left uncovered and are thus susceptible to dissolution.
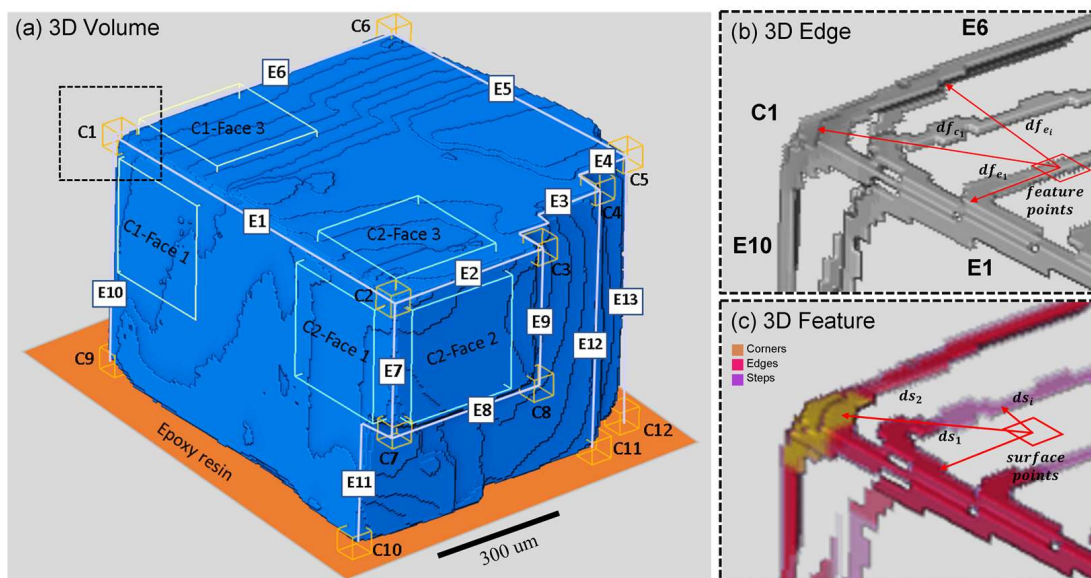

Figure 2. (**a**) Three-dimensional volume of the studied galena particle with the basal surface coated by epoxy resin (orange) and the other surfaces uncovered along with the chosen particle corners (C_1 to C_{12}), pseudo-edges (E_1 to E_{13}), and the selected regions of interest (labelled in succession C_1-Face$_1$ to C_2-Face$_3$), (**b**) Three-dimensional edge and illustration of the distance calculation from feature points (df_{c_i} and df_{e_i}), (**c**) Three-dimensional feature showing the classified macroscopic features (particle corners, steps and edges) and the illustration of distance calculation from surface points (ds_i) for the reactivity mapping.

2.2. Dissolution Experiment

The dissolution experiment was similar to the single particle leaching method applied by Winardhi et al. [26]. Accordingly, the galena particle moves freely in a stirred beaker filled with ethaline (Figure 3). The ethaline was chosen because it is an example of a deep eutectic solvent (DES), a group of promising green solvents that may be used in extractive metallurgy (e.g., ore leaching). DESs are widely regarded as "green" solvents, as they are typically biodegradable and have a low melting point. Some ore minerals (such as galena) have been shown to be highly soluble in certain DESs [4,26]. Ethaline was prepared by mixing 1:2 M ratio of choline chloride (ChCl, Sigma Aldrich, >98%) and ethylene glycol (EG, Merck, >98%) with 100 mM of iodine as a catalyst [4]. The solvent was then stirred at 500 rpm and heated to 50 °C in a closed container until a consistent mixture was obtained. By letting the galena particle move freely in the beaker, all points of the surface of the galena particle are assumed to be equally exposed to interaction with the ethaline solvent. The galena particle was scanned using CT prior to the dissolution experiments, and then it was scanned again in two-time steps of 8 h each of exposure to ethaline. The galena particle was rinsed each time, prior to CT scanning, using ethylene glycol in order to prevent precipitation of lead(II) chloride [30], followed by ethanol to remove ethaline residues.
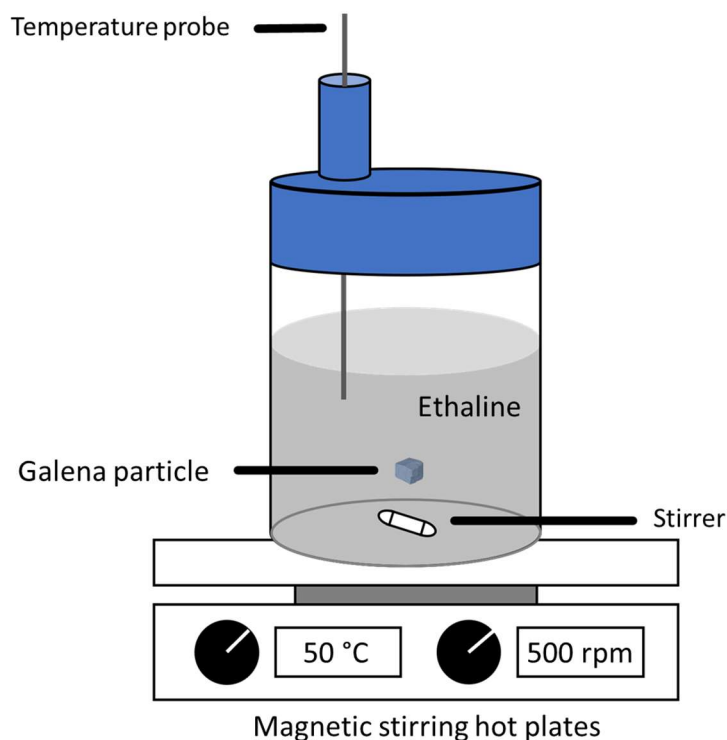

Figure 3. Illustration of the setup of the single particle leaching experiment used in this study. The galena particle was stirred in a beaker glass filled with ethaline at 50 °C and 500 rpm. Note that the galena particle moves freely within the beaker glass (similar to laboratory bulk leaching experiments), thus avoiding the effect of directional flow.

2.3. X-ray Micro-Computed Tomography (CT)

CT scanning was performed using a XRE CoreTOM (Tescan) instrument with a voxel size of 4.65 μm, X-rays with a maximum of 180 kV, 15 W power, 1500 ms exposure time, and a 50 μm tungsten filter mounted at the source to filter the X-ray beam. Radiographs were reconstructed using Acquila 1.0.0.70 reconstruction software supplied by Tescan. The three-dimensional images were processed using the Avizo 9.2.0 software package by applying an image processing workflow proposed by Noiriel et al. [23] to calculate the dissolution rate spectra. The three-dimensional volume of the particle during the different dissolution time steps was registered using the surface covered by epoxy resin as a reference.

Images were filtered using a non-local means algorithm, and they were segmented using the region growing algorithm. A Chamfer distance map was calculated to measure the surface retreat due to dissolution time steps. The dissolution rate spectra across the particle surface were obtained by masking of the distance map with the segmented particle prior to the dissolution experiment.

In order to calculate the bulk dissolution rate, the volume and surface area of the particle at each time step were calculated from the segmented data. The global bulk dissolution rate, k_i (mol·h^{-1}), was obtained by dividing the volume difference, $(V_{t_0} - V_{t_i})$, by the molar volume (v_{gal}) and time difference $(t_i - t_0)$ (Equation (1)) [22], while the normalized bulk dissolution rate, k_{norm_i} (μm·h^{-1}), was calculated by dividing the volume difference by the time interval and normalized using the average surface area (A_{t_0,t_i}) between two time steps (Equation (2)) [31]. The uncertainty of the bulk dissolution rate was estimated by dilating or eroding (6-connectivity) one voxel distance from the segmented particle mask.

$$k_i = \left(\frac{V_{t_0} - V_{t_i}}{t_i - t_0} \right) \cdot \frac{1}{v_{gal}} \tag{1}$$

and

$$k_{norm_i} = \left(\frac{V_{t_0} - V_{t_i}}{t_i - t_0} \right) \cdot \frac{1}{A_{t_0,t_i}} \tag{2}$$

2.4. Reactivity Mapping

In order to understand the relation between macroscopic features, such as corners or edges and dissolution rate spectra, a reactivity map was generated based on an empirical model. This reactivity map shows the contribution of one or more macroscopic features towards the adjacent crystal surfaces during the dissolution process. It is the underlying hypothesis that this reactivity can be calculated based solely on the particle geometry and that the reactivity map reflects the dissolution rate spectra. A code was developed using MATLAB MathWorks (code can be found in Supplementary Files) in order to generate the reactivity map. The segmented three-dimensional volume was used as an input, and then it was resliced as a two-dimensional image in the x-y, y-z, and x-z directions, followed by two-dimensional Sobel edge detection in order to obtain all relevant features points of the particle (Figure 2b). These step were performed in order to obtain all macroscopic features (feature points) within the particle. In order to classify these feature points into corners, edges or steps, a total of 13 points were chosen as initial corners (C_1 to C_{13}). Then, an imaginary line at the interception of these corner points was created, which acts as initial edges as illustrated in Figure 2a. These imaginary lines will be referred as pseudo-edges (E_1 to E_{14}). There were no pseudo-edges defined on the epoxy-coated surface of the galena particle, as this was assumed to be non-reactive during dissolution. Then, the distance between the corners and pseudo-edges towards the feature points (Figure 2b) was calculated as vectors in order to obtain the crystal corners and edges position within the three-dimensional volume. Thus, a three-dimensional volume showing the classified particle corners, edges and steps was obtained Figure 2c.

In the following, the distance of all voxels within the surface (surface points) towards the particle corners, edges, and steps was calculated by using the same distance calculation (Figure 2c). An additional constraint for steps was required during this calculation of distance, namely, that the model will only calculate the distance if step and surface points were located on the same terrace, e.g., the same elevation on the crystal surface. This relation most likely will have an exponential trendline for an atomic scale model [18,32]. The crystallographic effect was assumed to be indirectly included within the dissolution rate spectra measured at each point of the particle surface. Therefore, the data were fitted using Equation (3), where the dissolution rate spectra (k) in a surface point decreases as it moves away from a macroscopic feature (d_f) with an exponential relation constant ($-b$). The constant, c, represents the lowest point of the resultant exponential curve—and it can be interpreted as the minimum dissolution rate across the particle surface. On the other

hand, constant *a* is the point where the curve intersects with the y-axis ($d_f = 0$) that can then be interpreted as the maximum dissolution rate related to a specific macroscopic feature.

$$k(d_f) = a.exp^{(-b.d_f)} + c \tag{3}$$

By using sum of the exponential part from Equation (3) and the distance from a surface point (*f*) towards each macroscopic features (corners, edges and steps), (d_f), the reactivity map on a particle surface point (R_f) can be calculated, as shown in Equation (4)

$$R_{f_{(corner,edge,step)}} = \sum_{i}^{n} exp^{-b.d_{f_i}} \tag{4}$$

Moreover, in order to understand the influence of the distance from surface features, a total of six regions of interest (ROI) was selected with two corners C_1 and C_2 as reference corners (Figure 1a). Two of these ROIs were localized near C_1 (C_1-Face$_1$, C_1-Face$_2$, C1-Face$_4$). The other three were localized near corner C_2 on different particle surfaces (C_2-Face$_1$, C_2-Face$_2$, C_2-Face$_3$). All ROIs have the same size of $48 \times 48 \times 10$ pixel (223×223 µm) and also preserve surface topography. Then, the ROI was placed within 10 pixel (46.5 µm) diagonally from the corners C_1 and C_2. The distance between the data points towards C_1 and C_2 can be calculated and plotted against the dissolution rate spectra. Note that two simplifications were made during these steps. First, for a given ROI, only the distance to C_1 and C_2 was calculated in order to display the macroscopic feature interactions. Second, due to the variability of dissolution rate values within the same distance across the particle surface, average dissolution rates were calculated. These are displayed in the results section.

3. Results

In this section, the result on the bulk dissolution rate and the evolution of the overall particle volume in response to dissolution of galena in ethaline is presented. Then, the relation between macroscopic features and dissolution rates is presented, starting with the results of the whole particle and followed by the details of dissolution occurring at the corners (C_1 to C_8). Finally, dissolution within the six chosen ROIs is documented and related to the interaction of macroscopic features.

3.1. Dissolution Experiment

A qualitative comparison of regions with particularly high dissolution rates clearly illustrates the decrease in volume and surface area of the particle over time (Figure 4a). This coincides with marked changes of the appearance of corners and edges. Edge E_1 (Figure 4b), for example, is a distinct and straight line at t_0 that separates Face 1 from Face 3 (Figure 2a). These two faces are also marked by the presence of few cleavage steps. After 8 h of dissolution (t_1), the edge E_1 starts to develop stair-case morphology (yellow arrow), which continues to encroach further on the adjacent faces within the next 8 h (t_2). Very similar is the development at corner C_2 and edges E_2 and E_7 (Figure 4c). At t0, this region has a simple and well defined cubic cleavage shape (Figure 4c). After the initial stage of dissolution (t_1), however, the region displays a stair-case morphology that encroaches on the three surrounding surfaces (Faces 1–3; Figure 1a). Particularly strong dissolution at corner C_2 consumes surface steps (blue arrow), and steps closer to C_2 develop from a rather straight shape into a curved shape (purple arrow) through time (t_2).
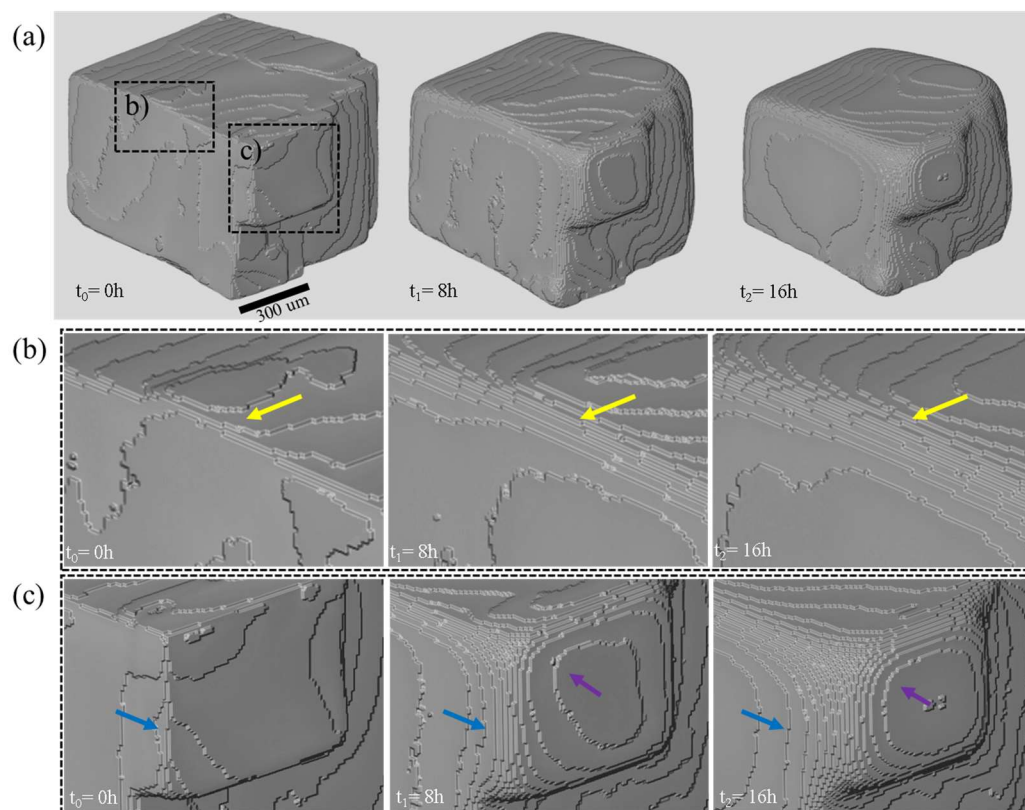
Figure 4. The three-dimensional volume rendering of the studied galena particle (**a**) overview of entire particle at different dissolution times. (**b,c**) Close-ups of selected regions on the particle. Notice that the yellow, blue, and purple arrows that point to particularly relevant changes in the particle morphology are describe in detail in the text.

Quantitatively, both volume and surface area decrease as the galena particle dissolves. The two dissolution rates calculated for the two time slices are rather consistent (Table 1). The uncertainty calculated by applying three-dimensional erosion and dilation resulted a maximum variation of 4% of the tabled value (data can be found on Supplementary Files Table S1). This is equivalent to a plus/minus one-voxel thick variation of the segmented mask of the particle. This is assumed here to be the main source of error in the measurement. The dissolution of the galena particle can, however, be much better visualized as dissolution rate spectra by calculating the surface retreat (Figure 5). The distribution of the dissolution rate shows the maximum rate of dissolution to decrease from 19 $\mu m \cdot h^{-1}$ for the first time step (t_1) to 16 $\mu m \cdot h^{-1}$ for the second time step (t_2). However, even though the surface area was smaller, the total surface area affected by dissolution (without counting the surface with 0 $\mu m \cdot h^{-1}$) increased (Figure 5). This is due to the fact that normalization required for bulk rate calculation assumes all surfaces to be reactive. Within the three-dimensional dissolution rate spectra (Figure 5), the dissolution was higher at corners, followed by dissolution along edges or surface steps (red-yellow tones, Figure 5), as can be expected [8,23]. Steps located closer to edges and corners have higher dissolution rates compared to steps located centrally on crystal surfaces.

Table 1. The bulk dissolution rates calculated using Equations (1) and (2) and three-dimensional image-derived quantities.

Time Step	Time (h)	Surface Area (µm^2)	Volume (µm^3)	k_i (mol·h^{-1})	k_{norm_i} (µm·h^{-1})
t_0	0	2.09×10^6	2.25×10^8	-	-
t_1	8	1.93×10^6	2.10×10^8	6.16×10^{-4}	0.97
t_2	16	1.81×10^6	1.94×10^8	6.23×10^{-4}	0.99
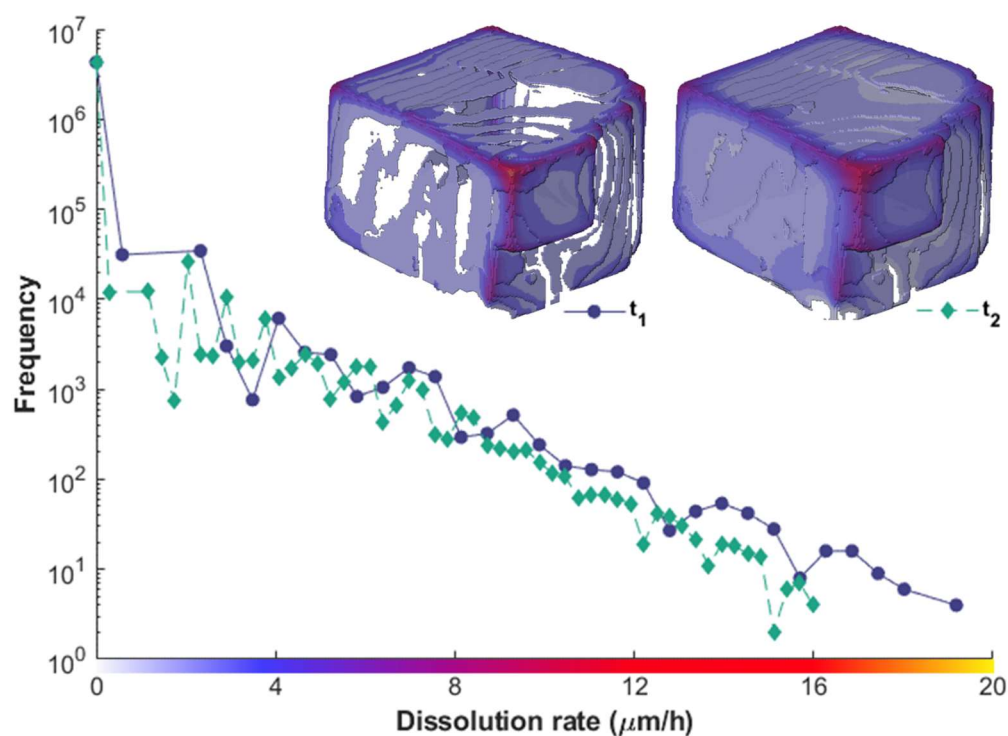
Figure 5. The distribution of the dissolution rate over the particle surface of t_1 (purple circle, continuous line) and t_2 (green diamond, dashed line) and the visualized three-dimensional dissolution rate spectra. Note that the dissolution rate in the grey areas is within the analytical uncertainty of 2 µm·h^{-1}. Dissolution in the white areas, on the other hand, is below the detection limit and thus is shown as 0 µm·h^{-1}.

Based on the calculation of a normalized bulk dissolution rate and assuming that dissolution was homogeneous across the entire surface of the galena fragment, a surface retreat of around 7.8 µm can be expected after 8 h of dissolution in ethaline for both time steps (t_1 and t_2). At a voxel size of 4.65 µm/pixels, this surface retreat will be equal to 1.7 pixels. As it is not possible to distinguish a surface retreat of 0.7 pixels, and considering the uncertainty inherent to segmentation and mis-registration of pixels, an uncertainty of ±1 pixel may be assumed. Thus, the maximum uncertainty of the surface retreat between the two dissolution time steps corresponds to a maximum analytical uncertainty of 2 µm·h^{-1}.

3.2. Relation of Macroscopic Scale Features and Dissolution Rate Spectra

The average dissolution rates for all corners, edges, or steps against the shortest distance towards each macroscopic feature show similar decreasing trendlines (Figure 6) for both t_1 and t_2. Note that this considers an average between all features marked in Figure 1 of the same type, e.g., all corners or all edges. This is a simplification that neglects the interaction between different macroscopic features. However, this was necessary to calculate a feature-specific constant (Table 2) for the reactivity map. In general, the average dissolution rate as a function of the distance from corners is faster compared the dissolution

rate at the same distance from edges and faces (Figure 6). The same is true for the maximum average dissolution rate. Comparing both time steps t_1 and t_2, both the maximum and minimum average dissolution rates of the macroscopic feature decreases through time (constant a and c, Table 2). Variability of the data around the best fit line is also obvious, especially for data obtained for corners, as these show high root mean square error (RMSE) relative to data for other macroscopic features. Nevertheless, the fitted line and the data are in a good agreement, as shown in Figure 6 and Table 2 (R-square (R^2) value above 0.90).
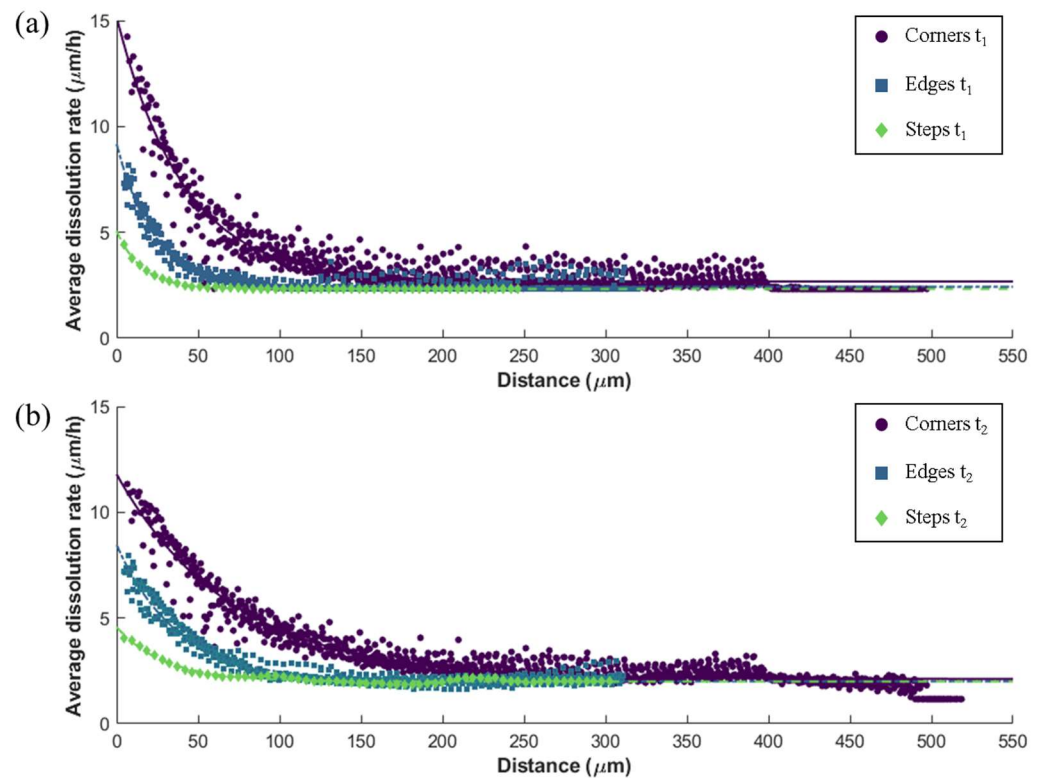
Figure 6. Plot of dissolution rates measured from the average of all corners identified in Figure 1 (purple circle, continuous line), edges (blue square, dotted line), and steps (green diamond, dashed line) vs. the distance from closest macroscopic feature (particle corner, edge or step) for both time steps (**a**) t_1 and (**b**) t_2.

Table 2. Fitting constants of Equation (3) for corners, edges, and steps, calculated from the exponential fitting of the average dissolution rate against distance.

Time Steps	Macroscopic Feature	a ($\mu m \cdot h^{-1}$)	b (μm^{-1})	c ($\mu m \cdot h^{-1}$)	R^2	RMSE
t_1	Corners	12.5	−0.0245	2.68	0.9054	0.5493
	Edges	6.75	−0.0441	2.44	0.9167	0.2952
	Steps	2.74	−0.0632	2.33	0.9982	0.0172
t_2	Corners	9.68	−0.0143	2.11	0.9353	0.4694
	Edges	6.45	−0.0268	2.00	0.9575	0.2597
	Steps	2.57	−0.0336	1.99	0.9634	0.09255

In order to provide more insight into the observed variability, Figure 7 shows a comparison of the average dissolution rates for each corner for the first time step (t_1). Similar to the average dissolution rate against distance plot (Figure 6), surfaces that are located close to corners show higher rates compared to those located further from corners. However, there are also significant differences of average dissolution rates between different corners: dissolution rates related to C_2 (Figure 7b) reach a maximum of ca. 20 $\mu m \cdot h^{-1}$,

whereas those related to C_8 (Figure 7h) only reach around 9 $\mu m \cdot h^{-1}$. The data variability can also be seen from the scattering and also the total data count that averaged into one value (brighter color display more data averaged and dark color display less data were averaged). The dissolution rates around C_1, C_2, C_5, and C_6 are more scattered around the fitting line in comparison to those of C_3, C_4, C_7, and C_8. The total dissolution rate data averaged into one value is higher between 100 and 300 μm of distance towards the corners. Figure 5i shows the comparison between the fitted line (continuous line) of all corners (C_1–C_8) and the total average (dashed line). It can be seen that there are significant deviations below 50μm distance towards the corners, and such deviations become smaller as the distance increases.
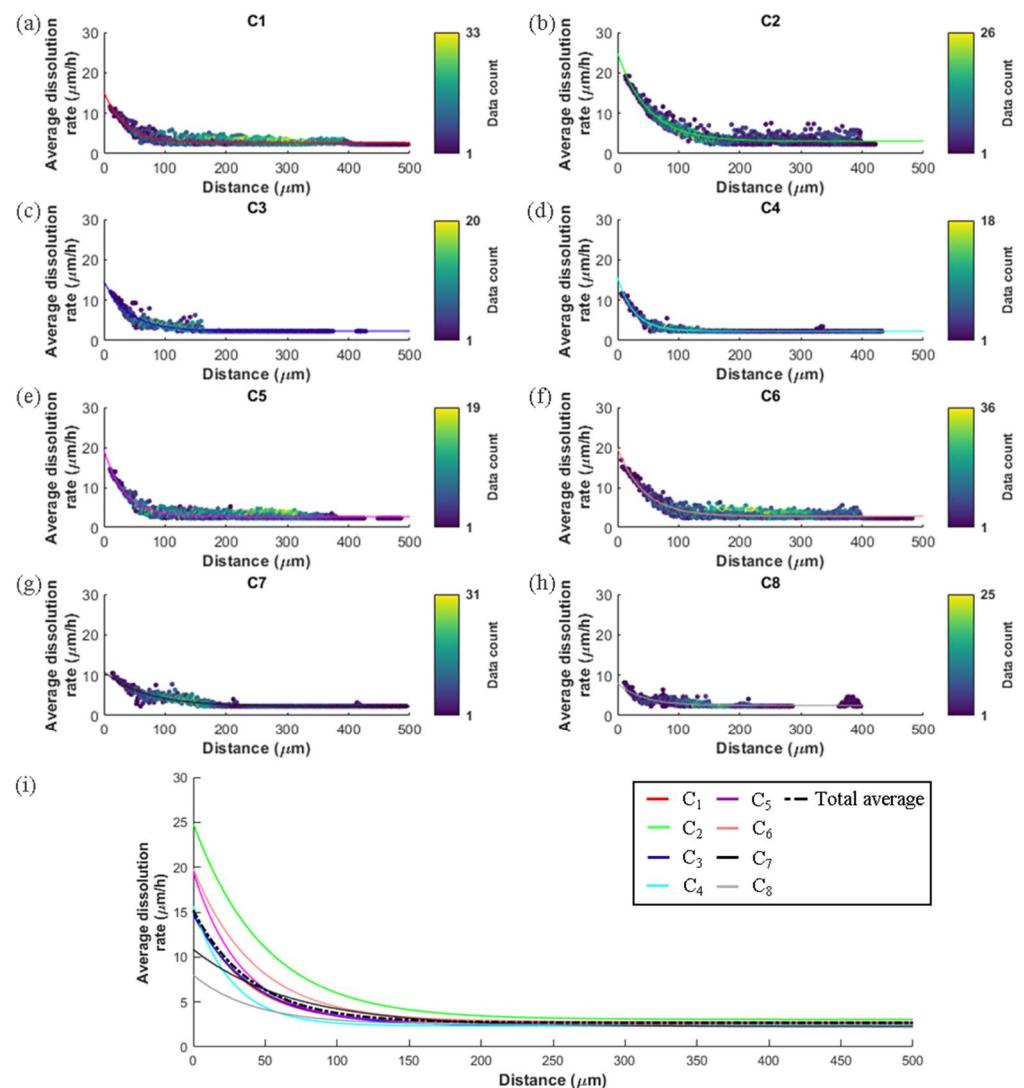
Figure 7. (**a–h**) Average dissolution rate data plotted against distance from a particular corner during the first time step (t_1). The color represents the amount of data that is averaged into one value (see legend). (**i**) Dissolution rate vs. distance lines obtained for individual corners (solid lines) compared to the total average (black dashed line).

To better understand the dissolution rate variability and the interaction of these with macroscopic features, a total of six ROIs were compared, and the dissolution rate spectra were plotted against the distance towards the C_1 and C_2 corners (Figure 8). It is obvious that the dissolution rates proximal to C_2 (Figure 8b) are greater compared to those proximal to C_1 (Figure 8a). Yet, dissolution rates approach a similar base line with increasing distance. Figure 8c illustrates that all dissolution rates approach similar values at a distance of

250 μm, with the notable exception of C_2-Face$_2$. For C_2-Face$_2$, the dissolution rate is not only particularly high overall, but an increase is observed at a distance of about 300 μm. A similar unexpected increase is observed between 200 μm and 250 μm distance for C_2-Face$_1$. These increases are related to the proximity and influence of other macroscopic features, in this case other corners. While the distance was only calculated towards corners C_1 and C_2, C_2-Face$_1$ is actually affected by C_7; C_2-Face$_3$, in turn, is affected by C_3. Significant shifts also mark the dissolution rate curve for C_2-Face$_2$ as it is affected by three corners, namely, C_3, C_7, and C_8. On the other hand, the dissolution rate curve for C_1 does not show similar shifts, as these remain unaffected be the influence of all other corners. C_1-Face$_3$, from about 100 μm distance, shows a small logarithmic decrement of the average dissolution rate, which can be attributed to small steps within the selected ROI of C_1-Face$_3$. These observations highlight the obvious fact that the dissolution of each surface (represented by ROIs here) is actually affected, not only by the closest macroscopic corner, but also by more distant corners.
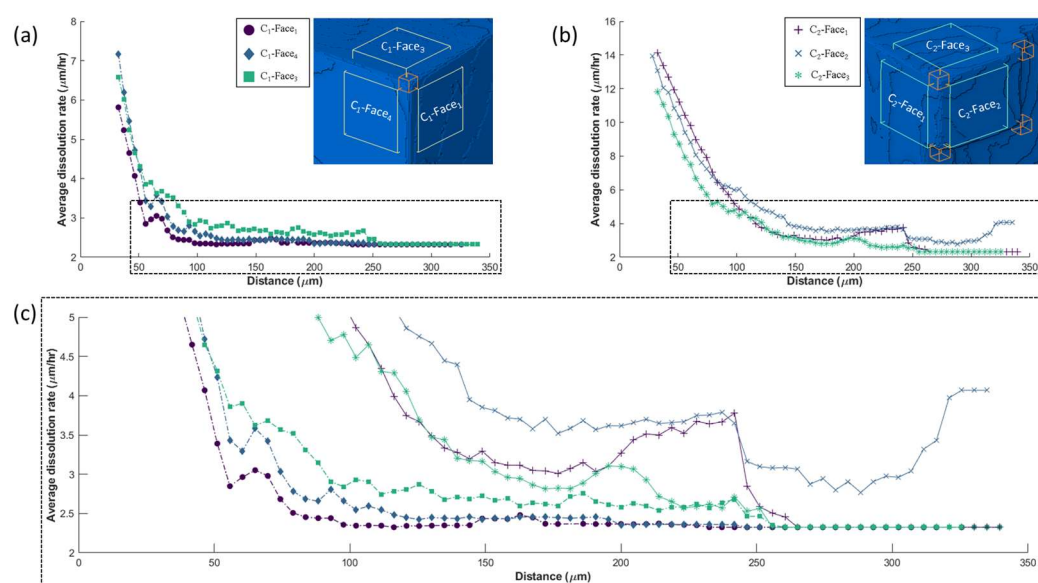

Figure 8. Comparison of the variation of the average dissolution rate within six ROIs around corner (**a**) C_1, (**b**) C_2, as a function of the distance to the feature. (**c**) Compare (**a**,**b**) to highlight the increasing dissolution rates around C_2 corner at distance between 200–250 μm in contract to the continuous decrease in the rates around C_1 corner.

3.3. Reactivity Mapping

Figure 9 shows the three-dimensional reactivity map that originates by applying the empirical relation of distance towards macroscopic features (Equation (4) and Table 2) for all points (voxels) of the surface as imaged by CT. The reactivity map illustrates the effect of macroscopic features towards neighboring faces, with surface reactivity decreasing markedly as distances from corners or edges increase. The area close to corners and edges displays the highest reactivity. It also shows the cumulative effect of nearby corners and edges, as seen in the most reactive part of the particle (C_2-Face$_2$, Figure 9b), which is the most reactive compared to the top (C_2-Face$_3$) and side (C_2-Face$_1$) parts. Furthermore, the model also captures the different reactivity of steps, as shown within the highlighted square in Figure 9b,c. Notice the white arrows (Figure 9b) as the reactivity within the steps correlates with the dissolution rate spectra. Similar to Figure 9b, the area surrounding edge E_1 (Figure 9c) is also visually in agreement with the rate map (black arrows). However, there are also differences between the reactivity map and the dissolution rate spectra. The reactivity map shows (as shown by red and yellow arrows) to have different reactivity within the surface. Dissolution rate spectra, on the other hand, suggest that the surface should have the same dissolution rate.
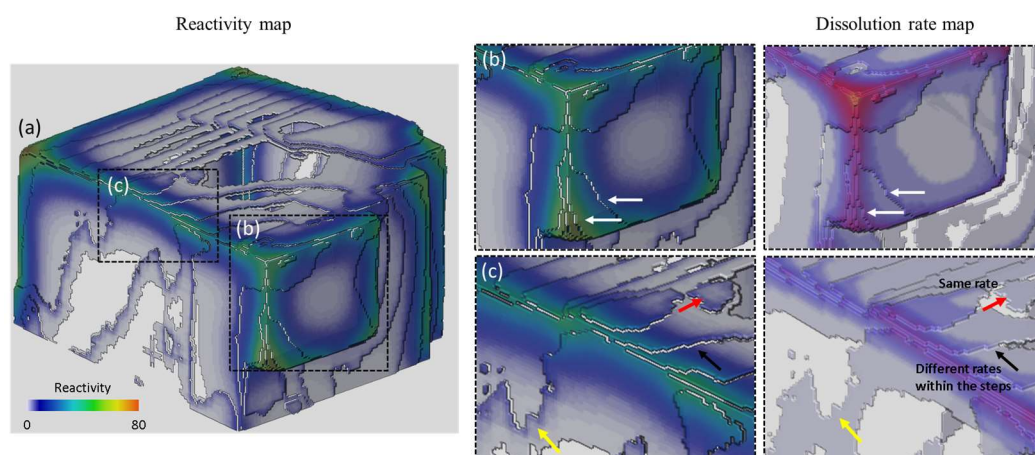
Figure 9. (**a**) Reactivity map for the studied galena particle at *t*0 based on the distance of all surface points towards macroscopic features. The highlighted square for (**b**,**c**) is the same illustrated in Figure 2b,c. Notice the black and white arrows that highlight close similarities between dissolution rate spectra and reactivity model, whereas red and yellow arrows point out locally, which represent remaining differences.

4. Discussion

The empirical reactivity model for the studied galena crystal is shown to be in good agreement (e.g., within the experimental uncertainty) with the dissolution rate spectra calculated from the available CT images (Figure 10). The reactivity map reproduces well the higher reactivity of particle corners and edges affecting the neighboring surfaces. With increasing distance of a selected point on a surface from particle corners or edges, the reactivity diminishes in an exponential manner, which leads to less dissolution or a low dissolution rate. Similarly, the reactivity map also captures differences in reactivity along the particle steps in the cleaved surfaces of the studied galena crystal relative to the macroscopic features (white and black arrows, Figure 9b,c). Additionally, the relation between these two variables shows a linear trendline with only little deviation (Figure 10). Considering a ±1 pixel uncertainty, both average values of t_1 and t_2 are still within the uncertainty range (the uncertainty bar overlaps for both time steps t_1 and t_2), which means the relation between these two variable persist over time. This implies that even though the macroscopic features attain a rounded shape during the dissolution process (Figure 4b,c), the reactivity and the effect towards neighboring surfaces remains similar. This is in agreement with observations documented in a previous study [11]. This supports the hypothesis that macroscopic features act as permanent sources of instability during mineral dissolution. This also means that the reactivity relation of Equation (4) can be used to predict the reactivity for successive time steps by using only the initial geometry of the dissolving galena crystal.
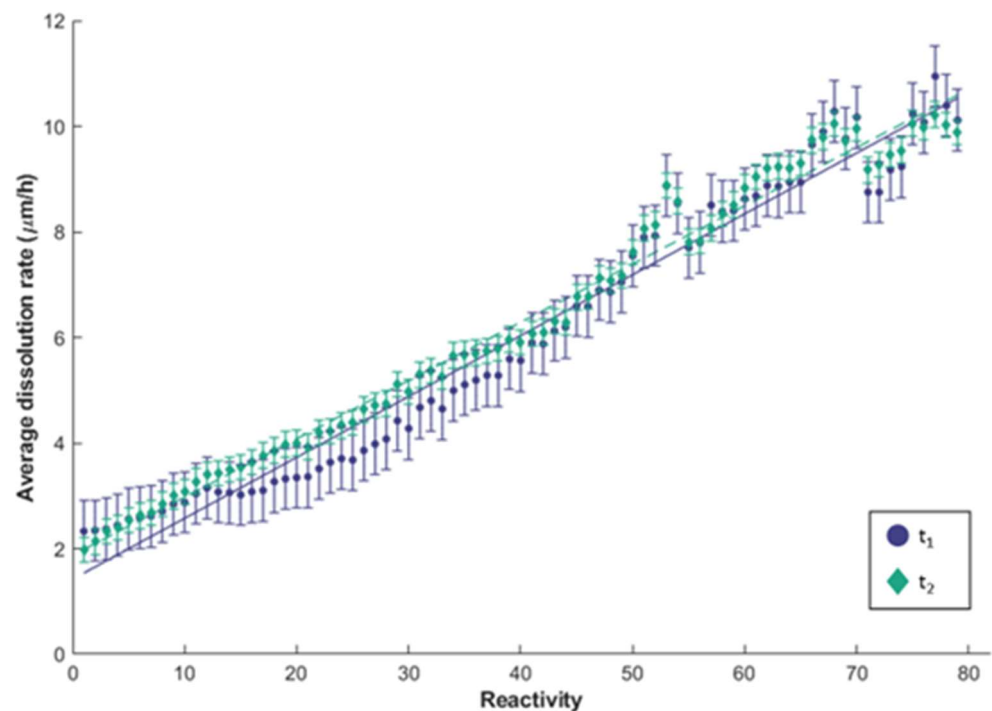
Figure 10. Relation between the computed reactivity with the measured average dissolution rates for t1 (purple circle) and t2 (green diamond), as well as the uncertainty of the measurement. Note the close fit of the linear regression lines for t1 (continuous line) and t2 (dashed line) with the uncertainty bars.

However, at the scales that can be resolved using CT, it is impossible to define the crystallographic orientation along particle corners and edges, as these become rounded during dissolution (Figure 4). Nevertheless, at the atomic level, every orientation between two {100} directions can be expected. The advantage of the proposed empirical model is that the additional reactivity of more reactive orientation is accounted without the necessity to resolve the orientation at each point. This is accounted for in the empirical relation between the measured dissolution rate spectra and the distance towards the macroscopic feature. This hypothesis is supported by Figures 9 and 10 that both document that the empirical model successfully captures the effect of macroscopic features at the interception of more than one particle planes (particle corners and edges) on the reactivity of the adjacent surfaces.

Yet, a dispersion of average dissolution rates between reactivity values 50–70 can be noted. This dispersion suggests locally greater variability, as shown also in Figure 5i. This variability is greater in surface areas that are located closed to particle corners. This leads to higher variability of dissolution rates at higher reactivity values. Moreover, the reactivity map (Figure 9c) shows the pointed features to have different reactivity within the surface (red and yellow arrow), while the dissolution rate spectra, on the other hand, display a similar dissolution rate.

The suggested reactivity map approach will certainly benefit ore leaching or batch mineral dissolution experiments, as it can provide constraints for the variability of dissolution rates based on the initial geometry of the particles in the studied material. In such bulk experiments, many particles with various geometry are simultaneously exposed to dissolution [33,34]. The geometry of these particles can be differentiated by calculating the distance of the surface towards relevant macroscopic features. This distance calculation can be computed from the three-dimensional images of the particles, which cannot be easily achieved using atomic-scale models. The empirical model may be further used to include the information about individual particle geometry in the variability of dissolution rate spectra. Additionally, it can be used as an input for mineral dissolution simulation instead

of using bulk dissolution rates (average of all particles). Thus, a better modelling condition of multi mineral particles during ore leaching could be applied (e.g., particle geometry effect and dissolution rate spectra) and, hence, this opens the possibility of optimizing ore leaching process.

5. Conclusions

The proposed empirical model for mineral dissolution successfully captures the effect of macroscopic features that intercept more than one surface (particle corners and edges) on the reactivity of adjacent surfaces. The model illustrates the exponential relation between dissolution rate and distance to macroscopic features, which ultimately is a consequence of atomic-scale reactions already described by mechanistic models. The proposed empirical model is also able to predict dissolution rate ratios between particle corners, edges, and steps based on the initial geometry of a studied particle, as well as the cumulative effect of the proximity of two or more macroscopic features to any point on a surface. This effect remains consistent over time, since during the dissolution of a three-dimensional object, the particle corners and edges persist as a source of increased reactivity towards the intercepting surfaces. This supports the initial hypothesis on which this study was based and illustrates that macroscopic features cannot be disregarded or compared to atomic scale surface features during mineral dissolution. Macroscopic particle features are distinct from atomic scale surface features by being persistent and predictable sources of dissolution. These findings demonstrate the importance of considering the entire particle geometry when trying to understand mineral dissolution.

References

1. Yadav, S.K.; Chakrapani, G.J. Dissolution kinetics of rock–water interactions and its implications. *Curr. Sci.* **2006**, *90*, 932–937.
2. Burton, M.; Bryant, S.L. Surface dissolution: Minimizing groundwater impact and leakage risk simultaneously. *Energy Procedia* **2009**, *1*, 3707–3714. [CrossRef]
3. Iglauer, S.; Paluszny, A.; Pentland, C.H.; Blunt, M.J. Residual CO_2 imaged with X-ray micro-tomography. *Geophys. Res. Lett.* **2011**, *38*, L21403. [CrossRef]
4. Jenkin, G.R.; Al-Bassam, A.Z.; Harris, R.C.; Abbott, A.P.; Smith, D.J.; Holwell, D.A.; Chapman, R.J.; Stanley, C.J. The application of deep eutectic solvent ionic liquids for environmentally-friendly dissolution and recovery of precious metals. *Miner. Eng.* **2016**, *87*, 18–24. [CrossRef]

5. Ilhan, S.; Akgün, D. Leaching Kinetics of Mo, Ni, and Al Oxides from Spent Nickel–Molybdenum Hydrodesulfurization Catalyst in H2SO4 Solution. *J. Sustain. Metall.* **2021**, *7*, 470–480. [CrossRef]

6. Dávila-Pulido, G.I.; Salinas-Rodríguez, A.; Carrillo-Pedroza, F.R.; González-Ibarra, A.A.; Méndez-Nonell, J.; Garza-García, M. Leaching kinetics of electronic waste for the recovery of copper: Rate-controlling step and rate process in a multisize particle system. *Int. J. Chem. Kinet.* **2021**, *53*, 379–389. [CrossRef]

7. Ruiz-Agudo, E.; Mees, F.; Jacobs, P.; Rodriguez-Navarro, C. The role of saline solution properties on porous limestone salt weathering by magnesium and sodium sulfates. *Env. Geol* **2007**, *52*, 269–281. [CrossRef]

8. Yuan, K.; Starchenko, V.; Lee, S.S.; de Andrade, V.; Gursoy, D.; Sturchio, N.C.; Fenter, P. Mapping Three-dimensional Dissolution Rates of Calcite Microcrystals: Effects of Surface Curvature and Dissolved Metal Ions. *ACS Earth Space Chem.* **2019**, *3*, 833–843. [CrossRef]

9. Agrawal, P.; Bollermann, T.; Raoof, A.; Iliev, O.; Fischer, C.; Wolthers, M. The contribution of hydrodynamic processes to calcite dissolution rates and rate spectra. *Geochim. Et Cosmochim. Acta* **2021**, *307*, 338–350. [CrossRef]

10. Godinho, J.; Piazolo, S.; Evins, L.Z. Effect of surface orientation on dissolution rates and topography of CaF$_2$. *Geochim. Et Cosmochim. Acta* **2012**, *86*, 392–403. [CrossRef]

11. Arvidson, R.S.; Ertan, I.E.; Amonette, J.E.; Luttge, A. Variation in calcite dissolution rates. *Geochim. Et Cosmochim. Acta* **2003**, *67*, 1623–1634. [CrossRef]

12. Fischer, C.; Kurganskaya, I.; Schäfer, T.; Lüttge, A. Variability of crystal surface reactivity: What do we know? *Appl. Geochem.* **2014**, *43*, 132–157. [CrossRef]

13. Luttge, A.; Arvidson, R.S.; Fischer, C. A Stochastic Treatment of Crystal Dissolution Kinetics. *Elements* **2013**, *9*, 183–188. [CrossRef]

14. Fischer, C.; Arvidson, R.S.; Lüttge, A. How predictable are dissolution rates of crystalline material? *Geochim. Et Cosmochim. Acta* **2012**, *98*, 177–185. [CrossRef]

15. Saldi, G.D.; Voltolini, M.; Knauss, K.G. Effects of surface orientation, fluid chemistry and mechanical polishing on the variability of dolomite dissolution rates. *Geochim. Et Cosmochim. Acta* **2017**, *206*, 94–111. [CrossRef]

16. Ruiz-Agudo, E.; Putnis, C.V.; Jiménez-López, C.; Rodriguez-Navarro, C. An atomic force microscopy study of calcite dissolution in saline solutions: The role of magnesium ions. *Geochim. Et Cosmochim. Acta* **2009**, *73*, 3201–3217. [CrossRef]

17. Godinho, J.R.A.; Gerke, K.M.; Stack, A.G.; Lee, P.D. The dynamic nature of crystal growth in pores. *Sci. Rep.* **2016**, *6*, 33086. [CrossRef]

18. Kurganskaya, I.; Trofimov, N.; Luttge, A. A Kinetic Monte Carlo Approach to Model Barite Dissolution: The Role of Reactive Site Geometry. *Minerals* **2022**, *12*, 639. [CrossRef]

19. Bibi, I.; Arvidson, R.; Fischer, C.; Lüttge, A. Temporal Evolution of Calcite Surface Dissolution Kinetics. *Minerals* **2018**, *8*, 256. [CrossRef]

20. Bollermann, T.; Fischer, C. Temporal evolution of dissolution kinetics of polycrystalline calcite. *Am. J. Sci.* **2020**, *320*, 53–71. [CrossRef]

21. Kahl, W.-A.; Yuan, T.; Bollermann, T.; Bach, W.; Fischer, C. Crystal surface reactivity analysis using a combined approach of X-ray micro-computed tomography and vertical scanning interferometry. *Am. J. Sci.* **2020**, *320*, 27–52. [CrossRef]

22. Noiriel, C.; Oursin, M.; Saldi, G.; Haberthür, D. Direct Determination of Dissolution Rates at Crystal Surfaces Using 3D X-ray Microtomography. *ACS Earth Space Chem.* **2019**, *3*, 100–108. [CrossRef]

23. Noiriel, C.; Oursin, M.; Daval, D. Examination of crystal dissolution in 3D: A way to reconcile dissolution rates in the laboratory? *Geochim. Et Cosmochim. Acta* **2020**, *273*, 1–25. [CrossRef]

24. Lin, Q.; Neethling, S.J.; Courtois, L.; Dobson, K.J.; Lee, P.D. Multi-scale quantification of leaching performance using X-ray tomography. *Hydrometallurgy* **2016**, *164*, 265–277. [CrossRef]

25. Noiriel, C.; Luquot, L.; Madé, B.; Raimbault, L.; Gouze, P.; van der Lee, J. Changes in reactive surface area during limestone dissolution: An experimental and modelling study. *Chem. Geol.* **2009**, *265*, 160–170. [CrossRef]

26. Winardhi, C.W.; Da Godinho, J.R.A.; Rachmawati, C.; Achin, I.D.; Iturbe, A.U.; Frisch, G.; Gutzmer, J. A particle-based approach to predict the success and selectivity of leaching processes using ethaline—Comparison of simulated and experimental results. *Hydrometallurgy* **2022**, *211*, 105869. [CrossRef]

27. White, A.F.; Brantley, S.L. The effect of time on the weathering of silicate minerals: Why do weathering rates differ in the laboratory and field? *Chem. Geol.* **2003**, *202*, 479–506. [CrossRef]

28. Lasaga, A.C.; Luttge, A. Variation of crystal dissolution rate based on a dissolution stepwave model. *Science* **2001**, *291*, 2400–2404. [CrossRef] [PubMed]

29. Lasaga, A.C.; Lüttge, A. A model for crystal dissolution. *Ejm* **2003**, *15*, 603–615. [CrossRef]

30. Spathariotis, S.; Peeters, N.; Ryder, K.S.; Abbott, A.P.; Binnemans, K.; Riaño, S. Separation of iron(iii), zinc(ii) and lead(ii) from a choline chloride-ethylene glycol deep eutectic solvent by solvent extraction. *RSC Adv.* **2020**, *10*, 33161–33170. [CrossRef] [PubMed]

31. Godinho, J.R.A.; Stack, A.G. Growth Kinetics and Morphology of Barite Crystals Derived from Face-Specific Growth Rates. *Cryst. Growth Des.* **2015**, *15*, 2064–2071. [CrossRef]

32. Rohlfs, R.; Fischer, C.; Kurganskaya, I.; Luttge, A. Crystal Dissolution Kinetics Studied by a Combination of Monte Carlo and Voronoi Methods. *Minerals* **2018**, *8*, 133. [CrossRef]

33.　Schulz, B.; Sandmann, D.; Gilbricht, S. SEM-Based Automated Mineralogy and Its Application in Geo- and Material Sciences. *Minerals* **2020**, *10*, 1004. [CrossRef]

34.　Godinho, J.R.A.; Grilo, B.L.D.; Hellmuth, F.; Siddique, A. Mounted Single Particle Characterization for 3D Mineralogical Analysis—MSPaCMAn. *Minerals* **2021**, *11*, 947. [CrossRef]